ACS OMEGA

http://pubs.acs.org/journal/acsodf
Article

Unveiling the Origin of Fast Hydride Ion Diffusion at Grain Boundaries in Nanocrystalline TiN Membranes

Yuji Kunisada,* Chiharu Kura, Norihito Sakaguchi, Chunyu Zhu, Hiroki Habazaki, and Yoshitaka Aoki

Cite This: *ACS Omega* 2024, 9, 13738−13745
Read Online

ABSTRACT: Nanocrystalline titanium nitride (TiN) has been determined to be a promising alternative to noble metal palladium (Pd) for fabricating base membranes for the energy-efficient production of pure hydrogen. However, the mechanism of transport of hydrogen through a TiN membrane remains unclear. In this study, we established an atomistic model of the transport of grain boundary hydride ions through such a membrane. High-resolution transmission electron microscopy and X-ray reflectivity confirmed that a nanocrystalline $TiN_{1.0}$ membrane with a (100) preferred growth orientation retained about 4 Å-wide interfacial spaces along its grain boundaries. First-principles calculations based on the density functional theory showed that these grain boundaries allowed the diffusion of interfacial hydride ion defects with very small activation barriers (<12 kJ mol^{-1}). This was substantiated by the experiment. In addition, the narrow boundary produced a sieving effect, resulting in a selective H permeation. Both the experimental and theoretical results confirmed that the granular microstructures with the 4 Å-wide interlayer enabled the transition metal nitride to exhibit pronounced hydrogen permeability.

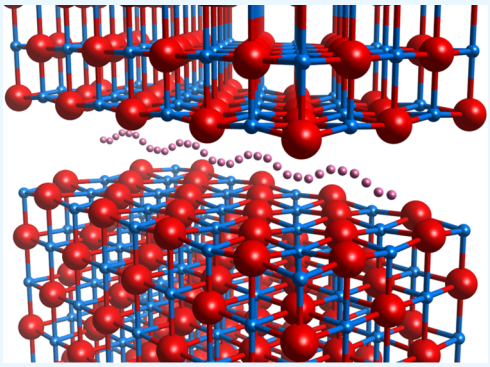

INTRODUCTION

The growing global energy crisis and increasing demand for clean and efficient energy sources have constrained a greater disposition to embrace the proposed "hydrogen economy" as a long-term solution.[1,2] Polymer electrolyte fuel cells, which are a major application of hydrogen technology, require an ultrapure fuel grade (99.995%) and can only tolerate parts per million concentrations of contaminants such as CO_2, CO, and CH_4 because they are capable of poisoning the utilized Pt catalysts. This has necessitated the need for the development of cost-effective methods for hydrogen purification and separation. Dense-membrane separation is the most feasible technique for producing ultrapure hydrogen owing to its low energy consumption, ease of operation, high yield, and cost effectiveness.[3] Palladium-based alloys have a strong potential for use in hydrogen purification owing to their combination of a high hydrogen permeability and excellent resistance to hydrogen embrittlement.[3−6] However, the resource scarcity of Pd strongly motivates the development of Pd-free alternatives to enable the development of more sustainable technology.

In more recent years, nanocrystalline membranes fabricated from titanium nitride (TiN), which is one of the toughest ceramics, have been found to exhibit pronounced hydrogen permeability, even at ambient temperatures. Although some metal oxides such as $BaZr_xCe_{0.8-x}Y_{0.2}O_3$ have been known to exhibit proton conductivity at elevated temperatures,[7,8] the hydrogen transport capability of TiN features mixed hydride ion and electron conductivity.[9,10] The nanocrystalline matrices are readily hydrogenated at ambient hydrogen pressure through the formation of Ti−H terminal groups on the individual crystallite surfaces. This results in hydridic diffusion along the interfacial grain boundary, aided by bond exchange between the Ti−H groups.[9] It has been determined that a 600 nm thick membrane yields a hydrogen permeation flux of 6×10^{-7} mol cm^{-2} s^{-1} under a pressure difference of about 50 kPa at ambient temperature. This flux is several orders of magnitude higher than that of an ultrathin Pd membrane, which is technologically limited to a thickness of 5 μm at the same temperature, and just 1 order of magnitude lower than the U.S. DOE target values for H-permeable membranes at 673 K.[11] Nanocrystalline TiN_x systems are thus promising Pd alternatives for dense separation membranes. Hence, it is of both fundamental and technological importance to understand more precisely the essential hydrogen transport mechanism of TiN_x, including the hydride ion hopping path, the thermodynamic reason for the hydridic defect, and the cause of the significantly lower diffusion energies.

In the present study, we developed a robust physical model of the grain boundary transport of hydride ions in nearly stoichiometric TiN nanocrystalline films and demonstrated

Received: October 21, 2023
Revised: February 26, 2024
Accepted: February 29, 2024
Published: March 15, 2024

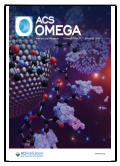

https://doi.org/10.1021/acsomega.3c08277
ACS Omega 2024, 9, 13738−13745

that the intergrain spacing at the boundaries was crucial to the occurrence of selective hydrogen permeation. In the case of TiN membranes formed from tens of nanometer-sized crystallites with a preferred (100) growth orientation, there is an interspace of a few ångströms between the (100) faces of the crystallites. This agrees with the critical values obtained by first-principles calculations based on spin-polarized density functional theory (DFT) of hydrogen solubility and permeability. We also examined the mechanism of the fast hydrogen diffusion at the grain boundary using DFT calculations.

METHODS

RF Sputtering of TiN Membranes. The stoichiometric TiN membranes were deposited by radio frequency (RF) reactive sputtering in an ultrahigh-vacuum chamber system (Ulvac ACS-3000) using a Ti disk target (99.99% purity) in a flow of pure N_2. The chamber pressure and RF power of the sputtering were fixed at 0.9 Pa and 195 W, respectively. To obtain membranes with varying crystallite sizes, the TiN crystal growth rate was controlled by varying the substrate temperature to 25, 200, and 500 °C, respectively. The thickness of the membranes was varied within 500−1000 nm by varying the sputtering time.

Hydrogen Permeability Measurement. The porous support was prepared using the method employed in our previous study.[9] Briefly, macroporous α-Al_2O_3 disks were prepared by uniaxial pressing of alumina powder followed by sintering at 1200 °C for 12 h in air. A mesoporous γ-Al_2O_3 layer was then deposited on the disks by sol−gel spin coating using a 0.6 M boehmite viscous precursor sol prepared by mixing a poly(vinyl alcohol) (PVA) solution and 1 M boehmite sol.[12,13] The TiN films were directly deposited on the porous alumina support by RF sputtering to obtain TiN membranes.

The hydrogen permeability of the TiN membranes was measured using a gastight chamber system built in-house, together with a gas chromatography system (GL Sciences GC-4000). The TiN membrane devices were sealed in a specially designed sample holder by using carbon sheet gaskets. Pure Ar gas was supplied to the porous support side at 25 sccm and a 1:1 gas mixture of H_2/N_2 was supplied to the membrane side at 100 sccm using mass flow controllers. Detection of H_2 and He in the outflow gas was performed using a thermal conductivity detector (TCD) with Ar and N_2 gas flows used as the reference.

Characterization. The phase purities were determined by X-ray diffraction (XRD; Rigaku RINT2200 Diffractometer with Cu Kα radiation). The measurements were performed by using 500 nm TiN films deposited on a Si wafer surface modified with a 100 nm mesoporous γ-Al_2O_3 layer. This enabled an investigation of the morphologies of the films on the porous alumina supports. The microstructures of the TiN membranes were characterized by transmission electron microscopy (TEM; JEOL JEM-2010F). The ultrathin specimens used for the high-resolution TEM were prepared using an Ar ion milling system (Gatan PIPS).

Magic angle spinning nuclear magnetic resonance (MAS NMR) spectroscopy was also performed by using a JEOL JNM-ECAII spectrometer. The employed powdered specimens were prepared by scrapping off 5 μm TiN films deposited on a γ-Al_2O_3/Si wafer. The scrap powder was filled into a sample tube in an H_2 atmosphere. The amounts of hydrogen dissolved in the nanocrystalline films were measured at 25 °C using a 5 MHz quartz crystal microbalance (QCM). The Au film electrode (1.32 cm^2) of the quartz crystal resonator was fully covered by 1 μm TiN membranes by RF sputtering deposition using a shadow mask. The amount of absorbed gas was determined by the shift of the resonance frequency when switching from pure Ar to 50%-H_2/Ar gas.

DFT Calculations. First-principles calculations based on spin-polarized DFT were used to investigate the hydrogen permeability at the TiN boundary. A Vienna Ab initio Simulation Package (VASP 5.4.1)[14−17] and the projector-augmented wave (PAW)[18,19] method was employed. As proposed by Hamada,[20] rev-vdW-DF2 was adopted as the exchange−correlation functional for accurate inclusion of the van der Waals interaction. A 500 eV cutoff was used to limit the plane-wave basis set, while a 6 × 6 × 1 Monkhorst−Pack special k-point grid[21] was applied to the first Brillouin zone sampling using the first-order Methfessel−Paxton smearing method[22] with σ = 0.2 eV and without compromising the computational accuracy. The lattice constants for the system were set based on the 4.247 Å equilibrium lattice constant theoretically predicted using rev-vdW-DF2 and a 25 × 25 × 25 k-mesh on the primitive unit cell for bulk TiN.

The TiN(100)/TiN(100) boundary model was constructed using one hydrogen atom and a six-layer 2 × 2 TiN(001) slab with a vacuum layer representing the boundary region as shown in Figure S1 because the (100) surface is the most energetically favorable to TiN. In the boundary model, all of the atoms, including the hydrogen atom, are relaxed until the forces on each atom fall below 0.02 eV/Å. We considered different values of the vacuum layer thickness (L), which correspond to the boundary width, ranging from 1.5 to three times the interlayer distance. After relaxation, the vacuum layer thickness ranged between 2.29 and 6.427 Å. The TiN(100) surfaces were also modeled by six layers of 2 × 2 TiN(100) slabs and a 15 Å vacuum layer. The bottom two layers were fixed in the model. We considered four initial hydrogen atom adsorption sites, namely, the Ti top, N top, hollow, and Ti−N bridge sites. We also examined the He diffusion to determine the gas separation properties. We considered the zero-point vibrational energy of the H and He atoms, calculated by harmonic approximation using the small displacement method.

To investigate the hydrogen permeability at the boundary, we considered the H diffusion barriers for two-step diffusion, i.e., diffusion from the surface to the boundary and within the boundary. The diffusion barrier between surface and boundary, which corresponds to the barrier height for interfacial dissolution (ΔE_{diss}) of H and He atoms, is defined as the total energy difference between a H or He atom on the surface and one at the boundary. Therefore, a negative diffusion barrier between a surface and a boundary corresponds to a diffusion barrier between a boundary and a surface. The diffusion barrier of grain boundary diffusion (ΔE_{GB}) is calculated using the climbing image-nudged elastic band (CI-NEB) method.[23] The zero-point vibrational energy in a transition state is considered as the sum of the corresponding vibrational energy of real number frequencies.

In this study, the electric dipole correction layer in the vacuum area of the surface model was set to compensate for the electric dipole interactions between consecutive slabs.[24,25] The electron transfer was investigated by Bader charge analysis.[26,27] Visualization for electronic and structural analysis (VESTA) was used to visualize the atomic models and electron density distributions.[28]

https://doi.org/10.1021/acsomega.3c08277
ACS Omega 2024, 9, 13738−13745

RESULTS AND DISCUSSION

Granular Microstructures of TiN Membranes. Nanogranular membranes have been successfully fabricated from single-phase NaCl-type TiN_x by reactive sputtering of a pure Ti metal target in a mixed N_2/Ar process gas, with the chamber pressure and sputtering power fixed at 0.9 Pa and 195 W, respectively.[9] In this framework, the nitrogen stoichiometry (x) could be adjusted mainly by controlling the mixing ratio of the process gas components (N_2 and Ar). Nitrogen vacancies decrease when the N_2 ratio in the mixture gases increases. In this study, we fabricated nearly stoichiometric $TiN_{1.0}$ membranes by reactive sputtering at various substrate temperatures under a 20 sccm flow of pure N_2 process gases. The crystallite size was found to decrease with decreasing deposition temperature.[9,10] Electron probe microanalysis (EPMA) confirms that all films have a nearly stoichiometric composition with Ti/N molar ratios equaling 1.03 ± 0.06, and include a small amount of O impurities with the O/Ti molar ratios being less than 0.04. Hereafter, the membranes deposited at the substrate temperatures of 25, 200, and 500 °C are denoted by $TiN_{1.0}$-25, $TiN_{1.0}$-200, and $TiN_{1.0}$-500, respectively.

The $TiN_{1.0}$ membranes exhibited a (100) preferred orientation, irrespective of the deposition temperature, as observed by X-ray diffraction (XRD) (see Figure S2). The full width at half-maximum (fwhm) values of the (100) peaks also increased with decreasing temperature, attributable to the reduced crystallite size at a lower deposition temperature. Using the Scherrer equation, the average grain size (d_{av}) values for $TiN_{1.0}$-500, −200, and −25 were determined to be 22, 12, and 8 nm, respectively, as summarized in Table 1.

Table 1. RF Reactive Sputtering Temperatures for Preparing $TiN_{1.0}$ Nanocrystalline Membranes and the Average Grain Size (d_{av}) of the Corresponding Membranes Deposited on γ-Al_2O_3/Si Wafers as Determined by XRD and TEM

sample name	substrate temperature/°C	d_{av} (XRD)/nm	d_{av} (TEM)/nm
$TiN_{1.0}$-500	500	22	20
$TiN_{1.0}$-200	200	12	12
$TiN_{1.0}$-25	25	8	9

Cross-sectional transmission electron microscopy (TEM) images in Figure 1a−c revealed that the TiN layer was composed of nearly cuboid crystallites measuring a few tens of nanometers. The d_{av} significantly decreased with decreasing deposition temperature, being 20, 12, and 9 nm for $TiN_{1.0}$-500, -200, and -25, respectively. These crystallite sizes determined by TEM are in good agreement with the d_{av} values determined by XRD, as shown in Table 1. A high-resolution TEM (HRTEM) image also revealed the existence of intergranular spaces a few ångströms wide between the (100)-oriented cuboids. Typical examples are shown in Figure 1d,1e. The corresponding power spectra obtained by fast Fourier transform (FFT) showed only diffraction spots on the (200) face of the NaCl-type phase, confirming the formation of a TiN(100)/TiN(100) boundary. The individual cuboid crystallites were separated from each other by a space twice the (200) lattice fringe, which corresponds to a lattice constant of TiN (0.424 nm).

The relative density of the $TiN_{1.0}$ membranes was evaluated by the X-ray reflectivity (XRR). The parameter was found to decrease with decreasing deposition temperature, with the values being 95, 91, and 84% for $TiN_{1.0}$-500, -200, and -25, respectively (see Figure 2a−c). Using the brick layer model shown in Figure 2d, in which the cubic grain cores are arranged in a simple cubic lattice of length d_{av} separated by homogeneous, free grain boundary layers of width ζ,[29] the density of the TiN brick layer with ζ = 0.424 nm was calculated to be 94, 90, and 86% for d_{av} values of 22, 12, and 8 nm, respectively, which closely agree with the observed densities. Together with the HRTEM results, the forgoing confirms that the sputter-deposited $TiN_{1.0}$ matrix retains wide spaces of a few ångströms at the TiN(100)/TiN(100) boundary. The intersecting grain boundary spaces act as three-dimensional networked channels for the hydride ions.

Grain Size Enhancement for Increased Hydrogen Permeability and Solubility. The formation of hydridic defects, i.e., Ti−H functional groups, was confirmed by ^{1}H nuclear magnetic resonance (NMR) spectroscopy.[30] In our previous work, hydrogenated TiN-500 exhibited a sharp NMR peak at 1.93 ppm, attributed to the hydride ions coupling with Ti cations.[9] The $TiN_{1.0}$-25 film in this study also had similar spectroscopic features, as seen in Figure 3; the film had a sharp peak at δ = 1.93 ppm, and a broad peak of the hydroxyl groups of the sacrificial mesoporous γ-Al_2O_3 layers centered at δ = 5 ppm. The former was identical to the hydrogen defects in TiN, with the peak intensity increasing with hydrogenation. The δ values were, however, different from those of the protonic hydrogens in Ti−NH (3.9 ppm)[31] and Ti−NH_2 (13.5 ppm).[32] These features confirm that hydridic hydrogen defects were dominantly formed in TiN, according to the following hydrogenation reaction

$$Ti_{Ti}^{x} + 1/2H_2(g) + e' \rightarrow (TiH)_{Ti'} \quad (1)$$

To determine the hydrogen permeability and selectivity of the TiN membranes, 50 vol %-H_2/He mixtures were applied to the surface of the membranes, and the gas that exited from the support side was analyzed by gas chromatography. The He flux (J_{He}) values for all of the membranes were very low, at least 2 orders of magnitude lower than the hydrogen permeation flux (J_{H_2}) values, despite the fact that He atoms are smaller than those of H_2, as seen in Figures 4 and S3. This shows that the observed hydrogen transport was not via pinholes or cracks. Together with the NMR results, the foregoing confirms that the TiN membranes allow hydrogen permeation by a hydridic conductivity.

A J_{H_2} for the 600 nm $TiN_{1.0}$ membranes in Figure 4, i.e., the hydrogen permeability of the membranes significantly increases with decreasing average crystallite size d_{av}. The J_{H_2} values for $TiN_{1.0}$ equally increase with a decreasing d_{av} for every temperature. In other words, the temperature dependence remains unchanged with decreasing d_{av}. This is evidence of interfacially controlled hydride ion diffusion in the nanocrystalline matrices. J_{H_2} exhibits an Arrhenius-type linear temperature dependence for $T \geq 150$ °C, and less so for $T \leq 100$ °C due to the reduced mobility of the hydridic ions resulting from the negative formation energy of the Ti−H groups. The ratio between the hydrogen and deuterium permeation fluxes, J_{H_2}/J_{D2}, through the $TiN_{1.0}$-25 membranes, was observed to be close to the reciprocal ratio of the root

https://doi.org/10.1021/acsomega.3c08277
ACS Omega 2024, 9, 13738−13745

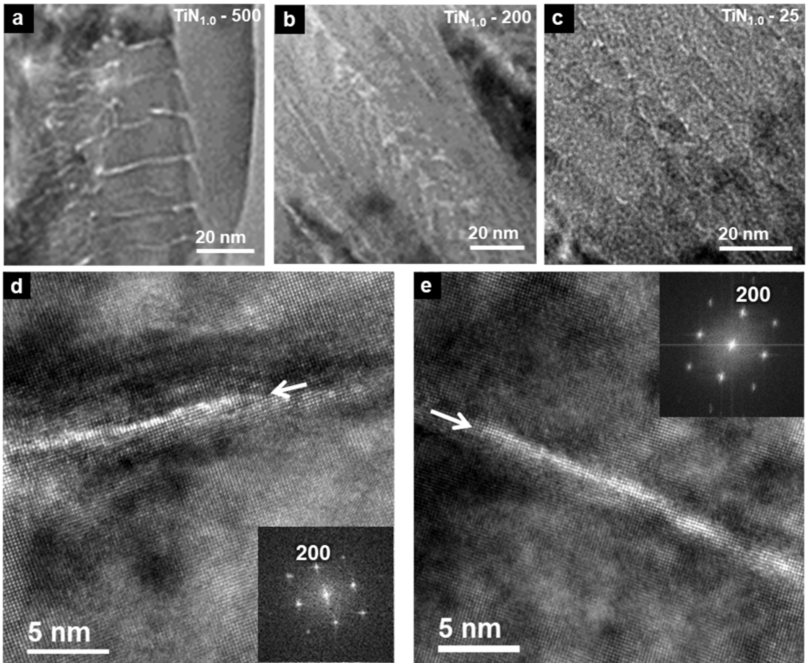

Figure 1. (a) Cross-sectional TEM image of a $TiN_{1.0}$ layer deposited at (a) 500, (b) 200, and (c) 25 °C. (d, e) Typical HRTEM image of the boundary region; insets are the corresponding power spectra obtained by FFT.

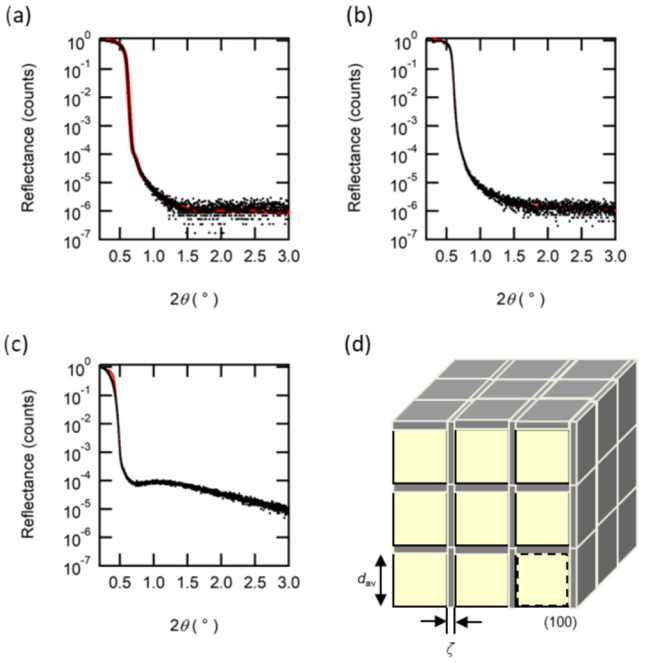

Figure 2. X-ray reflectivity (XRR) profiles of (a) $TiN_{1.0}$-500, (b) $TiN_{1.0}$-200, and (c) $TiN_{1.0}$-25. In (a–c), black dots show the observed and red lines show the simulations. (d) Schematic image of the brick layer model used for interfacial hydridic conduction in nanocrystalline NaCl-type metal nitride membranes; the yellow cubes represent grain cores, and the gray shells represent the grain boundary phase. Here, all of the square surfaces of each cubic grain core exhibit (100) crystallographic surfaces. d_{av} and ζ show the grain size and grain boundary width, respectively.

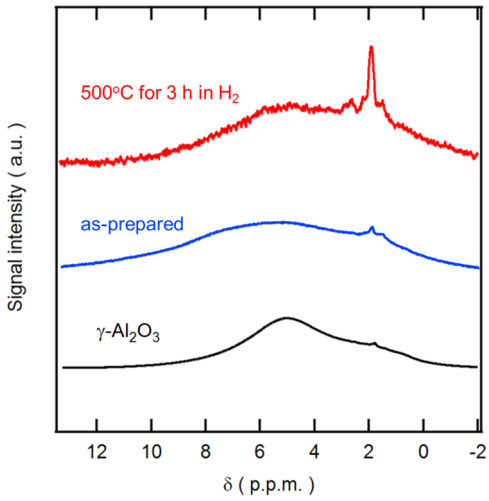

Figure 3. ^1H NMR spectra of $TiN_{1.0}$-25 films (1 μm thickness) detached from the Si substrate with a 100-nm-thick γ-Al_2O_3 sacrificial coating. Blue lines show the spectra of as-deposited films, and red lines show the films treated in 50 vol % H_2/Ar at 500 °C for 3 h. The spectrum of the sacrificial γ-Al_2O_3 layer (1 μm thickness) is also shown as a reference.

mass, $\sqrt{M_D}/\sqrt{M_H} \approx 1.4$ (see Figure S4), providing a signature of diffusion-limited hydrogen permeation.[33] Hence, the activation energy (E_a) at $T \geq 150$ °C should correspond to the diffusion energy of the hydridic defects, with the values for $TiN_{1.0}$-500, -200, and -25 being 12, 9.8, and 8.9 kJ mol^{-1}, respectively, as summarized in Table 2.

The room-temperature hydrogen sorptions of $TiN_{1.0}$-25 and −200 were measured using a 5 MHz quartz crystal microbalance (QCM) by directly depositing TiN films on the Au electrode of a quartz resonator at 25 or 200 °C, as seen in Figure 5.[34,35] Unfortunately, thermal damage made it difficult to deposit TiN_x-500 on the resonator. Upon the exposure of $TiN_{1.0}$-25 and -200 to 50%-H_2, the QCM frequencies abruptly dropped and stabilized at −27.4 and −20.2 Hz, respectively, which corresponded to 1.32 and 1.11 μg of hydrogen sorption at 25 °C, respectively. Using the geometric film volumes and ideal molar density (8.44×10^{-2}

https://doi.org/10.1021/acsomega.3c08277
ACS Omega 2024, 9, 13738−13745

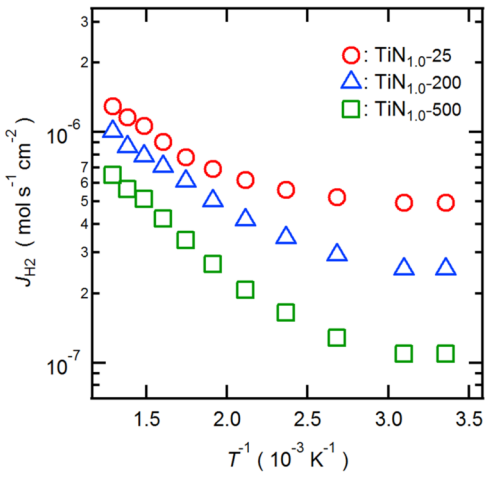

Figure 4. Arrhenius plots of hydrogen fluxes (J_{H_2}) through $TiN_{1.0}$ membranes of 600 nm thickness prepared at 25, 200, and 500 °C.

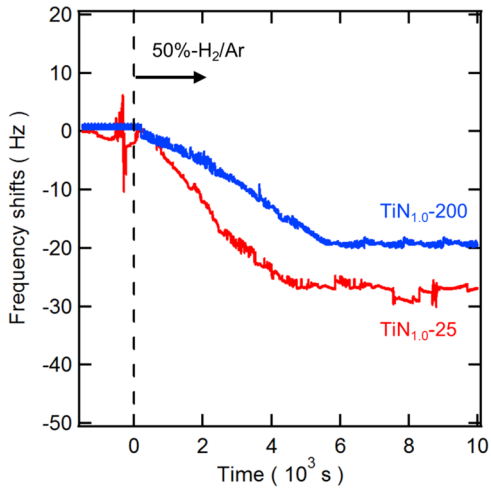

Figure 5. Response transient of QCM frequency shifts due to hydrogen adsorption on $TiN_{1.0}$ films (1.0 μm) deposited at 25 or 200 °C on a gold film oscillator electrode (1.32 cm^2). Measurements were performed by switching from pure Ar to 50 vol % H_2/Ar at 25 °C.

mol cm^{-3}),[36] the values of the hydrogen solubility (S_H), which is defined by the H/Ti ratio under equilibrium, of $TiN_{1.0}$-25 and −200 were calculated as 0.14 and 0.11, respectively. The determined S_H values are also summarized in Table 2. The TiN_x membranes thus contained smaller crystallites that tended to have a higher hydrogen solubility, with $TiN_{1.0}$ composed of crystallites measuring less than 10 nm yielding a 10^{-6} mol cm^{-2} s^{-1} hydrogen flux at 400 °C, as seen in Figure 4. This flux level is only 1 order of magnitude smaller than the DOE target.[11]

According to the brick layer model in Figure 2d,[37] the grain boundary volume of nanocrystalline TiN is proportional to the volumetric surface area, which is correlated with d_{av}^{-1}. Decreasing d_{av} from 12 (TiN-200) to 8 nm (TiN-25) increases the S_H by a factor of 1.4, which is in agreement with the inverse ratio of d_{av}, i.e., (8 nm/12 nm)$^{-1}$ ≈ 1.4. This unambiguously demonstrates that the hydridic defects are predominantly formed along the grain boundaries as Ti−H terminal groups on the individual crystallites, without being introduced into the grain interior.[9] In addition, the J_{H_2} ratios of $TiN_{1.0}$-200-to-$TiN_{1.0}$-500 and $TiN_{1.0}$-25-to-$TiN_{1.0}$-500 agree well with the inverse ratios of d_{av}, i.e., (12 nm/22 nm)$^{-1}$ ≈ 1.8 and (8 nm/22 nm)$^{-1}$ ≈ 2.5, respectively. This reveals that the concentration of the mobile hydride defect is linearly proportional to d_{av}^{-1}, as shown in Figure S5. These results show that hydridic conduction in nanocrystalline TiN is mediated by the interfacial grain boundary paths.

Mechanism of Hydride Ion Diffusion. The above results demonstrate that hydrogen transport in nanocrystalline TiN has an interfacial mechanism rather than a bulk mechanism that is mediated via vacancies or interstitials. To provide a more robust physical model, first-principles calculation was used to figure out the favored occupation sites and diffusion paths in the grain boundary region of the (100)-oriented TiN granular matrices. Ideally, (100)-growth-oriented NaCl-type cubes have six equivalent square faces on the (100) crystal plane so that the simple model of the TiN(100)/TiN(100) boundary can be represented by the face-to-face sandwiches of the (100) epitaxial layers.

Regarding the H adsorption on the TiN(100) surfaces (i.e., for L = 15 Å), the most stable adsorption site is the Ti top site. The hollow site is also a stable adsorption site, although its energy level is 44.7 kJ mol^{-1} higher than that of the Ti top site. The hydrogen adatom cannot stably adsorb at the N top and Ti−N bridge sites, and thus migrates to the Ti top site. The valence number of a hydrogen atom associated with Ti is about −0.6, which indicates that the hydrogen adatoms are converted into hydride ions. The corresponding Ti−H distance is 1.768 Å, which agrees well with the 1.84 Å sum of the ionic radii of Ti^{4+} and H^-.[38]

The barrier heights for the interfacial dissolution (ΔE_{diss}) of H and He atoms in Figure 6, defined as the ΔE_{ad} difference between the surface adatoms (L = 15 Å) and the interfacial adatoms (L < 15 Å), oscillate with decreasing boundary thickness L. The value of ΔE_{diss} decreases with decreasing L from 15 Å because the adatoms interact with both the top and bottom surfaces of the slabs, i.e., two TiN bricks, attaining a minimum value at L = 5.31 Å. However, ΔE_{diss} tends to increase with decreasing L to less than 5.31 Å, attributed to

Table 2. Summary of the Structural and Hydrogen Transport Properties of 600 nm $TiN_{1.0}$ Membranes Prepared at 25, 200, and 500 °C

sample name	d_{av} (XRD)/nm	crystal orientation	hydrogen flux at 500°C/mol cm^{-2} s^{-1}	hydrogen flux at RT/mol cm^{-2} s^{-1}	E_a of permeability/kJ mol^{-1}	hydrogen solubility, S_H
$TiN_{1.0}$-500	22	(100)	6.5×10^{-7}	1.3×10^{-7}	6.0 ($T \leq 100$ °C) 12 ($T \geq 150$ °C)	
$TiN_{1.0}$-200	12	(100)	1.0×10^{-6}	2.6×10^{-7}	6.1 ($T \leq 200$ °C) 9.8 ($T \geq 250$ °C)	0.11
$TiN_{1.0}$-25	8	(100)	1.3×10^{-6}	4.9×10^{-7}	6.1 ($T \leq 150$ °C) 8.9 ($T \geq 200$ °C)	0.14

https://doi.org/10.1021/acsomega.3c08277
ACS Omega 2024, 9, 13738−13745

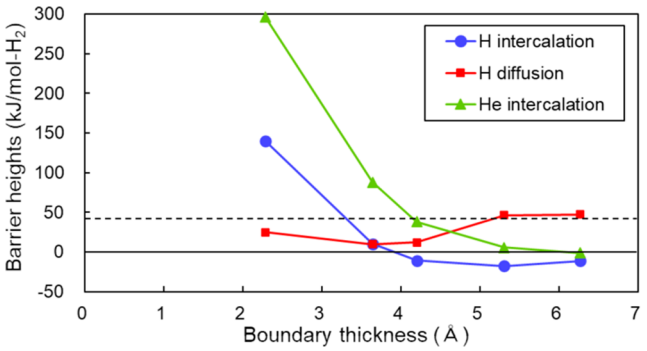

Figure 6. Boundary thickness (L) dependence of the barrier heights for interfacial dissolution and the grain boundary diffusion of H and He atoms. The dotted line shows the barrier height for the surface diffusion of the H atoms.

destabilization caused by the confinements in the small grain boundary. These results suggest that the incorporation of the hydridic defects into the grain boundaries is thermodynamically plausible when the grain boundary width is >3.65 Å.

The barrier height for the grain boundary diffusion (ΔE_{GB}) decreases with decreasing L to less than 6.27 Å, reaching a minimum around L = 3.65 Å, beyond which ΔE_{GB} begins to increase with further reduction of L due to the interspaces becoming too small for the hydride ions. The corresponding energy profiles through hydrogen diffusion are shown in Figure S6. Hence, only a relatively small ΔE_{GB} of about 9.9−12.1 kJ mol^{-1} is available in the L range of 3.65−4.20 Å, which agrees with the observed diffusion barriers of 6.0−12.0 kJ mol^{-1}. Because ΔE_{GB} varies with L, the temperature dependency of the diffusion barrier of TiN may be due to the differing grain boundary widths; hydrogen carriers prefer a path with a smaller barrier height. The present theoretical results are consistent with the HRTEM and XRR measurements, which reveal the formation of grain boundaries (intergrain spaces) 4 Å wide. The theoretical and experimental results demonstrate that the formation of hydridic hydrogen defects is energetically favored in the 4 Å-wide grain boundaries.

In contrast to H_2, the adsorption of He adatoms into the grain boundary is not energetically favored; ΔE_{diss} for He is higher than 88.3 kJ mol^{-1} for L < 3.65 Å. This indicates that the incorporation of He is not energetically favorable owing to the absence of an attractive interaction between the neutral He and charged Ti and/or N atoms. This theoretical observation agrees with the aforementioned experimental results, showing that nanocrystalline TiN matrices with 4 Å-wide grain boundaries do not allow the permeation of He atoms through molecular diffusion.

Finally, we examined the path of hydride ion hopping through the 4 Å-wide grain boundary interspaces. In the cases of grain boundaries more than 5.31 Å wide, a hydride ion could migrate from one Ti to a neighboring Ti with the lowest diffusion barrier via hollow site migration, as shown in Figure 7a. However, a N site in one grain would be close to a Ti site in another grain when the boundary width becomes 4.20 Å, resulting in hydride ion diffusion by intergranular transfer between the current Ti site and the Ti site in the other grain across the Ti−N bridge sites (Figure 7b). This modeling clarifies that achieving a balance between an attractive interaction with Ti and a repulsive one with N in 4 Å-wide grain boundaries can be used to create a pathway for hydride ions with a significantly reduced bottleneck at the grain

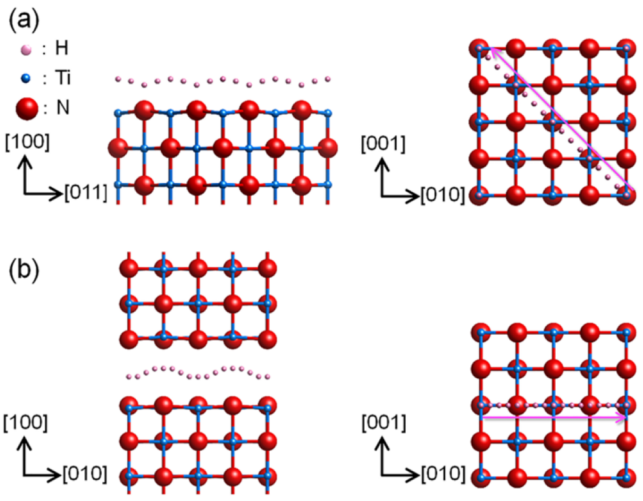

Figure 7. Top and side views of hydride ion diffusion paths (a) on TiN(100) surfaces and (b) in the grain boundary (L = 4.3 Å). Blue, red, and pink balls are Ti, N, and H atoms, respectively.

boundaries. As the width of the grain boundary decreases to 3.65 Å, the repulsive interaction with the N atoms of the other side becomes stronger, leading to diffusion of the Ti−N bridge site through the Ti site but keeping the small diffusion barrier. At the even narrower 2.29 Å-wide grain boundaries, the most stable hydrogen sites change to near-Ti sites, and the diffusion passes through hollow sites. The current results show that the 4 Å-wide grain boundary structure plays a crucial role in significantly reducing the kinetic energy of hydride ion conduction. Due to the toughness of TiN used as a hard-coating material and the diffusion mechanism where hydrogen diffuses only at the grain boundaries and not into the grain, the TiN nanocrystalline membrane is expected to have high durability.

CONCLUSIONS

We demonstrated that the H permeability of a $TiN_{1.0}$ nanocrystalline membrane was driven by the fast diffusion of hydridic defects at the loosely bound grain boundaries. The sputter-deposited nanocrystalline $TiN_{1.0}$ matrix was readily hydrogenated when exposed to hydrogen, and Ti−H terminal groups were formed over the surfaces of the individual crystallites, resulting in the incorporation of hydridic defects into the grain boundary regions. It was observed that the selective hydrogen permeability of $TiN_{1.0}$ could be realized only when the intergrain space is about 4 Å wide. In such a confined space, the hydrogen defects are stabilized by attractive interactions between the hydride ion defects and the Ti cations. Conversely, the formation of He defects does not offer any energy gain, owing to the absence of attractive interaction between the neutral He atom and the charged framework, resulting in the defects not being favorably incorporated into the grain boundary. Moreover, a fast diffusion pathway for hydride ions is developed in the intergranular space, with little prevailing bottleneck attributed to the balance between the attractive interaction of the hydride ions with the Ti cations and their repulsive interaction with the N anions. Nanocrystalline $TiN_{1.0}$ membranes with appropriate grain boundary spaces are thus capable of hydrogen transport with lower diffusion energy and have good potential for

https://doi.org/10.1021/acsomega.3c08277
ACS Omega 2024, 9, 13738−13745

application to high-throughput separation for the production of ultrapure hydrogen at ambient temperature.

■ ASSOCIATED CONTENT

Supporting Information

The Supporting Information is available free of charge at https://pubs.acs.org/doi/10.1021/acsomega.3c08277.

Atomic structure of grain boundary model; XRD patterns of TiN films; Arrhenius plots of Helium fluxes through TiN films; H/D isotope effect on hydrogen fluxes through TiN membrane; relationship between hydrogen flux and inverse of average grain size; and energy profile through hydrogen diffusion (PDF)

■ AUTHOR INFORMATION

Corresponding Author

Yuji Kunisada − *Center for Advanced Research of Energy and Materials, Faculty of Engineering, Hokkaido University, Sapporo 060-8628, Japan;* orcid.org/0000-0001-7743-5369; Email: kunisada@eng.hokudai.ac.jp

Authors

Chiharu Kura − *Graduate School of Chemical Science and Engineering, Hokkaido University, Sapporo 060-8628, Japan;* Present Address: Chiharu Kura: Kobe Steel, Ltd., 1-5-5 Takatsukadai, Nishi-ku, Kobe 651-2271, Japan

Norihito Sakaguchi − *Center for Advanced Research of Energy and Materials, Faculty of Engineering, Hokkaido University, Sapporo 060-8628, Japan;* orcid.org/0000-0002-2157-5319

Chunyu Zhu − *Faculty of Engineering, Hokkaido University, Sapporo 060-8628, Japan; School of Low-Carbon Energy and Power Engineering, China University of Mining and Technology, Xuzhou 221116, China;* orcid.org/0000-0002-5975-9308

Hiroki Habazaki − *Faculty of Engineering, Hokkaido University, Sapporo 060-8628, Japan;* orcid.org/0000-0002-7172-8811

Yoshitaka Aoki − *Faculty of Engineering, Hokkaido University, Sapporo 060-8628, Japan;* orcid.org/0000-0001-5614-1636

Complete contact information is available at: https://pubs.acs.org/10.1021/acsomega.3c08277

Notes

The authors declare no competing financial interest.

■ ACKNOWLEDGMENTS

This work was supported by the JST MIRAI "Realization of a low carbon society, global issue" area, no. JPMJM17E7; JSPS KAKENHI: Grant-in-Aid for Scientific Research (B), no. 18H02066, JSPS KAKENHI: Grant-in-Aid for Young Scientists (B), no. 17K14114, and the "Nanotechnology Platform" program of the MEXT Japan. C.K. was supported by MEXT Japan through the "Ambitious Leader's Program" (Hokkaido University). This work was done using the facilities of the Supercomputer Center, the Institute for Solid State Physics, University of Tokyo.

■ REFERENCES

(1) Pellow, M. A.; Emmott, C. J. M.; Barnhart, C. J.; Benson, S. M. Hydrogen or batteries for grid storage? A net energy analysis. *Energy Environ. Sci.* **2015**, *8*, 1938−1952.

(2) Cornaglia, L.; Múnera, J.; Lombardo, E. Recent advances in catalysts, palladium alloys and high temperature WGS membrane reactors: A review. *Int. J. Hydrogen Ener.* **2015**, *40*, 3423−3437.

(3) Ockwig, N. W.; Nenoff, T. M. Membranes for Hydrogen Separation. *Chem. Rev.* **2007**, *107*, 4078−4110.

(4) Al-Mufachi, N. A.; Rees, N. V.; Steinberger-Wilkens, R. Hydrogen selective membranes: A review of palladium-based dense metal membranes. *Renewable Sustainable Energy Rev.* **2015**, *47*, 540−551.

(5) Luo, W.; Ishikawa, K.; Aoki, K. High hydrogen permeability in the Nb-rich Nb−Ti−Ni alloy. *J. Alloys. Compd.* **2006**, *407*, 115−117.

(6) Adams, B. D.; Chen, A. The role of palladium in a hydrogen economy. *Mater. Today* **2011**, *14*, 282−289.

(7) Kreuer, K. D. Proton-Conducting Oxides. *Annu. Rev. Mater. Res.* **2003**, *33*, 333−359.

(8) Iwahara, H.; Asakura, Y.; Katahira, K.; Tanaka, M. Prospect of hydrogen technology using proton-conducting ceramics. *Solid State Ionics* **2004**, *168*, 299−310.

(9) Kura, C.; Kunisada, Y.; Tsuji, E.; Zhu, C.; Habazaki, H.; Nagata, S.; Müller, M. P.; de Souza, R. A.; Aoki, Y. Hydrogen separation by nanocrystalline titanium nitride membranes with high hydride ion conductivity. *Nat. Energy* **2017**, *2*, 786−794.

(10) Kura, C.; Fujimoto, S.; Kunisada, Y.; Kowalski, D.; Tsuji, E.; Zhu, C.; Habazaki, H.; Aoki, Y. Enhanced hydrogen permeability of hafnium nitride nanocrystalline membranes by interfacial hydride conduction. *J. Mater. Chem. A* **2018**, *6*, 2730−2741.

(11) U. S. Department of Energy. U. S. Department of Energy Hydrogen, Fuel Cells, and Infrastructure Technologies Program, Multi-Year Research, Development and Demonstration Plan. 2007.

(12) de Vos, R. M.; Verweij, H. High-Selectivity, High-Flux Silica Membranes for Gas Separation. *Science* **1998**, *279*, 1710−1711.

(13) Uhlhorn, R. J. R.; Zaspalis, V. T.; Keizer, K.; Burggraaf, A. J. Synthesis of ceramic membranes. *J. Mater. Sci.* **1992**, *27*, 527−552.

(14) Kresse, G.; Hafner, J. *Ab initio* molecular dynamics for liquid metals. *Phys. Rev. B* **1993**, *47*, 558−561.

(15) Kresse, G.; Hafner, J. *Ab initio* molecular-dynamics simulation of the liquid-metal−amorphous-semiconductor transition in germanium. *Phys. Rev. B* **1994**, *49*, 14251−14269.

(16) Kresse, G.; Furthmüller, J. Efficient iterative schemes for *ab initio* total-energy calculations using a plane-wave basis set. *Phys. Rev. B* **1996**, *54*, 11169−11186.

(17) Kresse, G.; Furthmüller, J. Efficiency of ab-initio total energy calculations for metals and semiconductors using a plane-wave basis set. *Comput. Mater. Sci.* **1996**, *6*, 15−50.

(18) Blöchl, P. E. Projector augmented-wave method. *Phys. Rev. B* **1994**, *50*, 17953−17979.

(19) Kresse, G.; Joubert, D. From ultrasoft pseudopotentials to the projector augmented-wave method. *Phys. Rev. B* **1999**, *59*, 1758−1775.

(20) Hamada, I. van der Waals density functional made accurate. *Phys. Rev. B* **2014**, *89*, No. 121103.

(21) Monkhorst, H. J.; Pack, J. D. Special points for Brillouin-zone integrations. *Phys. Rev. B* **1976**, *13*, 5188−5192.

(22) Methfessel, M.; Paxton, A. T. High-precision sampling for Brillouin-zone integration in metals. *Phys. Rev. B* **1989**, *40*, 3616−3621.

(23) Henkelman, G.; Uberuaga, B. P.; Jónsson, H. A climbing image nudged elastic band method for finding saddle points and minimum energy paths. *J. Chem. Phys.* **2000**, *113*, 9901−9904.

(24) Neugebauer, J.; Scheffler, M. Adsorbate-substrate and adsorbate-adsorbate interactions of Na and K adlayers on Al(111). *Phys. Rev. B* **1992**, *46*, 16067−16080.

(25) Makov, G.; Payne, M. C. Periodic boundary conditions in *ab initio* calculations. *Phys. Rev. B* **1995**, *51*, 4014−4022.

(26) Bader, R. F. W. *Atoms in Molecules: A Quantum Theory*; Oxford University Press: New York, USA, 1990.
(27) Tang, W.; Sanville, E.; Henkelman, G. A grid-based Bader analysis algorithm without lattice bias. *J. Phys.: Condens. Matter* **2009**, *21*, No. 084204.
(28) Momma, K.; Izumi, F. *VESTA* 3 for three-dimensional visualization of crystal, volumetric and morphology data. *J. Appl. Crystallogr.* **2011**, *44*, 1272−1276.
(29) Kim, S.; Avila-Paredes, H. J.; Wang, S.; Chen, C.-T.; De Souza, R. A.; Martin, M.; Munir, Z. A. On the conduction pathway for protons in nanocrystalline yttria-stabilized zirconia. *Phys. Chem. Chem. Phys.* **2009**, *11*, 3035−3038.
(30) Hayashi, K.; Sushko, P. V.; Hashimoto, Y.; Shluger, A. L.; Hosono, H. Hydride ions in oxide hosts hidden by hydroxide ions. *Nat. Commun.* **2014**, *5*, No. 3515.
(31) Roesky, H. W.; Bai, Y.; Noltemeyer, M. Synthesis and Structure of $[\{(\eta^5\text{-}C_5Me_5)Ti(NH)\}_3N]$, a Titanium Imide Nitride. *Angew. Chem., Int. Ed.* **1989**, *28*, 754−755.
(32) Abarca, A.; Gómez-Sal, P.; Martín, A.; Mena, M.; Poblet, J. M.; Yélamos, C. Ammonolysis of Mono(pentamethylcyclopentadienyl) Titanium(IV) Derivatives. *Inorg. Chem.* **2000**, *39*, 642−651.
(33) Bonanos, N.; Huijser, A.; Poulsen, F. W. H/D isotope effects in high temperature proton conductors. *Solid State Ionics* **2015**, *275*, 9−13.
(34) Aoki, Y.; Hashizume, M.; Onoue, S.; Kunitake, T. Determination of Surface Area and Porosity of Small, Nanometer-Thick Films by Quartz Crystal Microbalance Measurement of Gas Adsorption. *J. Phys. Chem. B* **2008**, *112*, 14578−14582.
(35) Uekawa, N.; Kaneko, K. Nonstoichiometric Properties of Nanoporous Iron Oxide Films. *J. Phys. Chem. B* **1998**, *102*, 8719−8724.
(36) JCPDS Powder Diffraction File 38−1420.
(37) Schlom, D. G.; Chen, L.-Q.; Pan, X.; Schmehl, A.; Zurbuchen, M. A. A Thin Film Approach to Engineering Functionality into Oxides. *J. Am. Ceram. Soc.* **2008**, *91*, 2429−2454.
(38) Chertihin, G. V.; Andrews, L. Reactions of Laser Ablated Ti Atoms with Hydrogen during Condensation in Excess Argon. Infrared Spectra of the TiH, TiH_2, TiH_3, and TiH_4 Molecules. *J. Am. Chem. Soc.* **1994**, *116*, 8322−8327.

https://doi.org/10.1021/acsomega.3c08277
ACS Omega 2024, 9, 13738−13745